PhD in Information Technology and Electrical Engineering

Università degli Studi di Napoli Federico II

PhD Student: Shomnath Bhowmick

XXIX Cycle

Training and Research Activities Report – Third Year

Tutor: Giovanni Breglio – Co-Tutor: Giuseppe Coppola

Personal Information:

Name: *Shomnath Bhowmick*

Masters: *University of Sheffield and University of Leeds, United Kingdom.*

Doctorate: *XXIX Cycle- ITEE – Università di Napoli Federico II, Napoli, Italy*

Fellowship type: *Research fellowship at IMM-CNR , Napoli, Italy*

Tutor: *Giovanni Breglio* **Co-Tutor:** *Giuseppe Coppola*

Study and Training Activities:

Courses:

Number Of courses	Credits Awarded
Euro Progettazione	**3**
National Instrument training	**3**
Three core issues for the internet: things, security and economic	**2**
GE2015 PhD school	**4**
AFM/EFM specialist course	**4**
An introduction to physics of nanostructures	**4**
Integrated Photonics	**3**
A lung-on chip to measure oxygen affinity of single red blood cells	**4**
Scientific Writing Course	**5**
Total	**32**

Seminars:

Number Of seminars	Credits	Date	Number of Hours (Hrs)
Luce e future	**1.6**	**1/12/2014**	**4+4**
Horizon 2020 I progetti Europei nella prospettiva di Un valutatore Eu (CNR)	**0.8**	**11/11/2014**	**4**
Biotechnologie industriali	**0.8**	**30/01/2015**	**4**
Secondo convegno nazionale sensori	**1.6**	**19/03/2014**	**4+4**

Engineering electromagnetic fields at the nanoscale	**0.4**	**26/10/2014**	**2**
Keys to getting your papers published	**0.4**	**15/09/2015**	**2**
Label-free imaging and characterization of bovine sperm cells: a combined holographic and spectroscopic approach.	**0.8**	**18/06/2015**	**4**
Laser emission devices and methods for CARS-based spectroscopy of electroporated biological cells	**0.8**	**22/05/2015**	**4**
Development of an automated microfludic platform for multiplexing in flurosecence analysis	**0.8**	**20/06/2016**	**4**
Digitization, digital restoration, and visualization of antiquities: medieval manuscripts and scrolls from Herculaneum	**0.4**	**04/03/2014**	**2**
Setting Up a lattice Light-sheet Microscope	**0.4**	**01/06/2016**	**2**
Frontier in single Molecule Manipulation and Imaging of DNA-protein transactions	**0.8**	**22/01/2016**	**4**
A lung-on chip to measure oxygen affinity of single red blood cells	**0.4**	**11/06/2014**	**2**
Quantum Simulation with Integrated photonics	**0.8**	**17/03/2014**	**4**
Applications of Optical Eigenmodes in biophotonics	**0.8**	**25/03/2014**	**4**
Porou silicon: From optoelectronics devices to an innovative bio-analytical tool	**0.8**	**11/03/2014**	**4**

Export of cargo from the Endoplasmic Reticulum is regulated by a control system	**0.8**	**02/03/2016**	**4**
Total	**13.6**		**68**

Conference/ workshops:

1) Capri EOS tropical meeting 2015 17th September -19th September.
2) Toriono fotonica conference 6th- 8th may 2015.
3) GE Siene Conference 22nd-24th June 2015
4) Rome nano-italy conference 23/09/2015 (8hrs)
5) Toulose France NMDC conference 09th-12th October 2016

Tutorship:

AFM/ EFM for Maters students

1) Capri project: 4 hours (2 hrs theory+2 hrs practical) 08/09/2015
2) STEPFAR project : 4 hours (2 hrs theory+2 hrs practical) 21/09/2015
3) CERVIA project: 4 hours (2 hrs theory+2 hrs practical) 20/10/2015
4) STEPFAR project : 4 hours (2 hrs theory+2 hrs practical) 26/10/2015

Student: Name Surname	**Tutor: Name Surname**	**Cycle**
shomnath.bhowmick@unina.it	giovanni.breglio@unina.it	**XXIX**

	Credits year 1								**Credits year 2**								**Credits year 3**									
		1	2	3	4	5	6			1	2	3	4	5	6			1	2	3	4	5	6			
	Estimated	bimonth	bimonth	bimonth	bimonth	bimonth	bimonth	**Summary**	**Estimated**	bimonth	bimonth	bimonth	bimonth	bimonth	bimonth	**Summary**	**Estimated**	bimonth	bimonth	bimonth	bimonth	bimonth	bimonth	**Summary**	**Total**	**Check**
Modules	**18**					3	2	**5**	**9**		7	4				**11**	**13**	4		4			8	**16**	**32**	**30-70**
Seminars	**13**	4.4	0.4	0	0.4	2.4	0.8	**8.4**	**6**	0	1.6	0	0.4	0	0.8	**2.8**	**3**	0.8	1.2	0.4	0	0	0	**2.4**	**14**	**10-30**
Research	**34**	6.8	5	7	6	9	5	**39**	**42**	3	5.5	2	9	6	5	**31**	**42**	6.8	5.5	9	6	0	0	**27**	**97**	**80-140**
	65	11	5.4	7	6.4	14	7.8	**52**	**57**	3	14	6	9.4	6	5.8	**44**	**58**	12	6.7	13	6	0	8	**46**	**142**	**180**

Research Title: **Investigation of the Pyroelectric Fields generated by $LiNbO_3$ Induced by Integrated Microheaters**

Summary

The work focuses on the investigation of the pyroelectric effect from the –Z surface of Lithium ($LiNbO_3$) crystal using different microheater (µH) designs fabricated on the +Z surface of the crystal. Thermal analyses of the microheater designs were performed both theoretically and experimentally using COMSOL™ Multiphysics and FLIR SC7000 thermocamera respectively. The pyroelectric effect was investigated analyzing the current impulses detected using a metallic probe detector connected to an oscilloscope. The temperature variation induced by the microheater causes a spontaneous polarization in the crystal resulting in the formation surface bound charges. The electric field generated between the probe and the crystal surface causes the charge emission that appears as a voltage impulse on the oscilloscope. In an ambient condition, the air layer act as a dielectric thin film layer at few hundreds of microns between the detector probe and crystal surface gap spacing. It was demonstrated and validated that the threshold field strength require to generate the PE was near the dielectric breakdown of air. The pyroelectric emission shows a higher dependency on the rate of thermalization of the microheater and also the electric field generated between the probe to surface gap spacing's of crystal. The deep characterization of µHs is investigated, in order to demonstrate the reliability and the effectiveness of these microdevices for all those applications where compact and low-power consuming electrical field sources are highly desirable. Furthermore, the pyroelectric effect activated by the fan microheater was investigated analyzing the pyroelectrical current impulses detected using a micrometric metallic probe connected to an oscilloscope under humid conditions. A resistive Aluminum Sensor was integrated along the microheater in order to control the temperature variation effect from the microheater.

Keywords: P*yroeletric Fields, Lithium Niobate, Microheaters, COMSOL ™, Joules Effect, thermal Effect analysis*

I. Introduction

Pyroelectricity is the ability of certain materials to generate an electrical potential in response to a temperature change. This change in temperature induces a slightly movement of the molecules within the material that changes their dipole moments. Thus, two oppositely charged faces are created and an electrical field across the material is established. In other words, the pyroelectric effect is due to the dependence of the spontaneous polarization (Ps), the dipole moment per unit volume of the material, on the temperature. Historically, the most important applications of the pyroelectric effect have been related to the possibility to measure the power generated by a radiation source (pyrometry, infrared imaging, radiometry) [**Error! Bookmark not defined.**-4]. However, there are other applications that are growing in importance; such as: lithography [5,6], electrohydrodynamic effect based devices [7], electron emission devices [8,9], ion source spectrometry [10,11], aligning nano-particles in electrode free approach [12], nano droplet drawing [13,14]. In these applications, macroscopic thermal stimulation techniques (laser beam, hot plate, soldering iron rod) have been used to induce a switching of the polarization of the pyroelectrical material domains. Thus, these techniques

are based on cumbersome, heavy, expensive and power consuming systems that could also require well-experienced operators. Still, the spatial temperature distribution and its gradient are not always easy to control. In this paper, we describe a simple methodology to induce and control the pyroelectric effect, which has the potentiality of eliminating the aforementioned limitations and enabling the possibility of integration in microdevices. Specifically, we use a microheater realized on the bottom surface of the pyroelectric crystal. This approach, which has been widely investigated in other fields of application (thermo optical switches, chemical sensors, gas sensors, flow sensors and MEMS) [15-17], offers various advantages such as: low power consumption, small size, shaping of the temperature distribution and possibility of in situ control and monitoring. Moreover, the miniaturization of the microheater can avoid heating of the entire crystal, so enabling the possibility of array configuration.

In this paper, simulated and experimental results from the study of the pyroelectric effect (PE) induced by microheater realized on a Z-cut lithium niobate ($LiNbO_3$) crystal are presented. In particular, we report on four microheater designs (meander, fan, spiral and S-shape) that were fabricated on +Z surface of $LiNbO_3$ crystal using photolithography and thin film deposition technique [18]. Thermal and electrical analyses of these microheater designs were performed theoretically and experimentally, respectively. Steady state and transient regimes were investigated to better understand the thermal behaviour of different heater designs.

The pyroelectric effect activated by the microheater was investigated analysing the pyroelectrical current impulses detected using a micrometric metallic probe connected to an oscilloscope. In particular, the temperature variation due to the microheater induces a spontaneous polarization change, which produces a redistribution of the bound charges on the crystal surface. The electrical field generated between the crystal surface and the metallic probe causes an air breakdown that appears as an impulse on the oscilloscope. Generally, when a $LiNbO_3$ crystal is heated under ambient conditions, free charges in the air will readily compensate the change in the polarization, thereby avoiding the creation of an electric field [19]. Although, when the probe is few hundreds of microns far from the crystal surface where the air acts as a thick dielectric layer and the generated electric field strength between tip and surface is greater enough for induce an air breakdown. In this paper, the pyroelectric current impulses were analysed for different microheater designs and operating conditions in order to demonstrate the effectiveness of the microheater as thermal tool for activating the pyroelectric effect. In particular, we validate that the threshold electric field strength required to generate the current impulses at oscilloscope is approximately 3×10^6 V/m (dielectric breakdown of air). Current impulses with larger amplitude is detected above this threshold field strength while the impulses gradually disappears below the afore-mentioned threshold.

The carried out results could be particularly useful for applications that exploit the activation of an electrical field between the crystal surface and non-conducting region; such as: 3D lithography [20], aligning nano particles in electrode free [12], nano-droplet drawing [13,14].

II. Method and Fabrication

Four microheater designs, illustrated in Fig. 1, were analysed to evaluate the pyroelectric effect induced by different temperature spatial distributions. Microheaters were fabricated on +Z surface of $LiNbO_3$ crystal using titanium as a joule heating resistor material due to titanium oxide layer formation on exposed surfaces that results in the thermally and electrically stable microheaters [21]. Moreover, its conductivity allows using low drive voltage for useful heat generation. The possibility to realize the microheater directly on the surface of

the pyroelectric material allows maximizing the heat transmission towards $LiNbO_3$ crystal, thus minimizing heat conduction loss.

a. *Numerical simulation of microheaters*

The electro-thermal analysis of the microheaters was investigated using COMSOL™ Multiphysics [22]. All microheaters occupies an area 350µm × 350µm with a titanium thick layer of 300nm. In the full 3D numerical model, a $LiNbO_3$ substrate with a size of 10mm × 10mm × 500µm was considered.

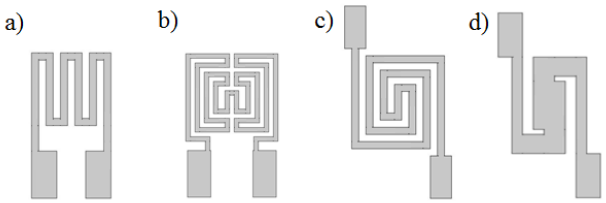

Fig1. Microheater designs a) Meander, b) Fan, c) Spiral, and d) S shape

The simulations were performed by coupling the power generation, due to the joule heating, with the heat conduction and dissipation into the device considering also the heat exchange with the surrounding air. The multiphysics simulation uses the electric current module in combination with the heat transfer module. The joule heating was calculated as a consequence of the input voltage, V_{pot} applied to the heaters pads. In particular, the electrical conductivity of the microheater, σ was modelled using a temperature dependent equation:

$$\sigma = \frac{1}{\rho_o*(1+\alpha(T-T_0))} \quad \ldots\ldots\ldots\ldots\ldots (1)$$

Where, ρ_0 is the resistivity at a reference temperature T_0, and α is the temperature coefficient of the resistivity that takes in account the dependence of the resistivity on the temperature.

In order to evaluate the heat transfer in the pyroelectric material, several material properties both of the $LiNbO_3$ and titanium (Ti) are required. Moreover, since the electrical and thermal properties of thin film materials differ from the bulk material properties, some of the titanium properties were specifically evaluated. In particular, the thermal conductivity of 300nm-thick film of titanium was considered to be 16.8 $Wm^{-1}K^{-1}$ [23]. This value is lower than the thermal conductivity of bulk materials (21.9 $Wm^{-1}K^{-1}$) due to the fact that, thermal transport of atoms is lowered as a result of the phonon scattering at lattice imperfections and boundaries [24]. Similarly, the electrical conductivity decreases due to the increase in thin film resistivity, occurring because of the low mean free path of the conduction electrons due to high scattering effect [25]. The electrical resistivity of our titanium thin films was evaluated (using four-point probe measurement) to be 2.85 µΩ·m. In Table I, all the parameters used for the heat transfer simulations are listed.

Parameter	**Titanium**	**$LiNbO_3$**
Heat capacity at constant pressure (C_p) [J/kg*K]	522	628

Electrical Resistivity (ρ) [μΩ·m]	2.85	2.63×10^{14}
Density (rho) [kg/m^3]	4506	4700
Thermal conductivity (k) [W/(m*K)]	16.8	5.6
Surface emissivity (ε)	0.60	0.35

Table I: Material properties of the heater and pyroelectric substrate ($LiNbO_3$).

Both steady state and transient analyses were performed. The joule heating was simulated as a result of an input voltage V_{pot} applied to the heater's pads. In time dependent study, a square voltage pulse was applied to switch the heater on and off at different time intervals. The heat transfer problem was solved considering Dirichlet, Neumann and mixed boundary conditions, and under the following realistic assumptions:

(i) Natural convective heat transfer was assumed for both sides of the $LiNbO_3$ surface and bottom surface of microheater, towards the surrounding environment (which is modelled as air with a constant temperature of $27°C$).

(ii) The thickness of the $LiNbO_3$ (500 μm) was much higher than the thickness of microheater (300nm); hence, to reduce the mesh complexity and minimize the modelling error, independent meshing procedures were considered for the different geometric structures. On the microheater upper surface, triangular 2D meshing is used with a minimum element size of 0.13mm and using a swept layer that mesh was projected along the thickness, resulting in 3D layered mesh. In $LiNbO_3$ volume a 3D tetrahedral meshing is considered with the minimum element size of 0.4mm;

(iii) In heat transfer physics; the heat dissipated from the surface of $LiNbO_3$ and microheater is greater than the heat dissipated from the vertical sides of the crystal. Hence, we can neglect the heat dissipation from the lateral surfaces by considering there a thermally insulated boundary condition [26].

(iv) In electric current physics, the contact resistance between microheater pads and connecting are considered negligible.

(v) Radiate heat power is proportional to the fourth power of temperature and hence makes a considerable amount of contribution in thermal exchange process. The physics was applied on the surfaces (top and bottom) of $LiNbO_3$ and microheater by applying a diffuse layer with the surface emissivity of $LiNbO_3$ and microheater material shown in Table I. There is no known literature work performed on the surface emissivity of $LiNbO_3$, thus experimental analysis were performed to evaluate its value. A two-point calibration procedure was adapted in order to evaluate the surface emissivity using an IR camera based set-up [27]. It was estimated that the $LiNbO_3$ surface emissivity was in a range between 0.5-0.65 at an ambient temperature.

The activation of pyroelectric effect by the microheater and the related induced electrical field was simulated using COMSOL™ Multiphysics. In particular, the steady state electric field formation between the –Z surface of $LiNbO_3$ crystal and a metallic probe tip was investigated. In Fig. 2 the simulated structure is sketched. A beryllium metallic probe tip was considered with a height dimension of 1.5 mm and a probe tip radius of 1μm. The tip was electrically grounded and immersed in air. The electrical field between the tip and the pyroelectric crystal depends on the electrical potential build up on the surface of crystal in response to a temperature variation. In particular, the electrical potential is related to the temperature variation ΔT by equation 2 [10]; i.e.:

$$V = d_{cr} * \gamma * \Delta T / \varepsilon_{cr} \quad \ldots\ldots\ldots\ldots\ldots\ldots (2)$$

Where, d_{cr} is the crystal thickness, γ=8.2nC*cm^{-2}* K^{-1} and ε_{cr}=31 are the pyroelectric coefficient and the dielectric constant of $LiNbO_3$ along z-axis, respectively. COMSOL simulator was used to estimate the electrical field distribution around the tip as function of the gap between the tip and the $LiNbO_3$ surface. In particular, this gap was varied from 100µm to 1mm.

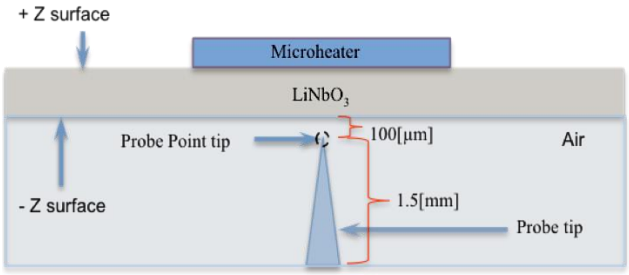

Fig 2. Design used for the electric field simulation between probe tip and –Z surface of LiNbO3 crystal.

b. *Fabrication*

Fabrication of the four different designs was performed in four-step process (see Fig. 3): cleaning, photolithography, thin film deposition and lift off process. A 3-inch single domain Z-cut $LiNbO_3$ crystal (0.5mm) was cut is parts of 10mm × 10mm; each part was cleaned in acetone, DI water and IPA for 10 min using a sonication bath.

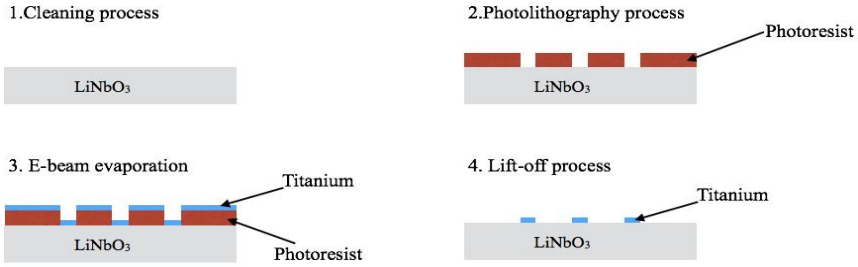

Fig.3. The schematic fabrication process of the micro-heater

The +Z face $LiNbO_3$ surface was spin coated with OIR-906 12i positive photoresist followed by the photolithographic patterning. Subsequently, the photoresist was baked for 2 min at 95°C, the geometric patterns were developed using OPD-4624 developer for 1min. In the second step of fabrication, we used electron beam evaporation technique for depositing 300nm thick titanium films onto the patterned $LiNbO_3$ +Z surface. Then a lift off process was performed in acetone for 20 min using the sonication bath. Finally the pads of the microheater were wire bonded using silver paste. In table II both the simulated and measured resistance for the realized microheater is reported, showing a good agreement between the data.

Design	Simulated resistance [Ω]	Measured Resistance [Ω]
Meander	365	373
Fan	807.5	818
Spiral	695	707
S shape	130	137

Table II. Simulated and measured resistance obtained for different microheater designs.

III. Simulation and experimental results

a. *Thermal analysis of the microheater*

Thermal analysis of the microheater designs were performed using COMSOL simulator and an infrared setup [28]. The core of the IR system is the FLIR SC7000 camera equipped with a 640×512 InSb sensors focal plane array. The acquired simulated thermal maps and the relative profiles along the line AA' from the –Z surface of $LiNbO_3$ are reported in Fig. 4 and Fig. 5 respectively.

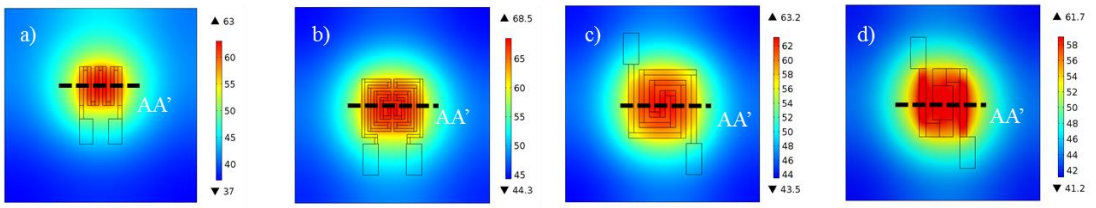

Fig 4. COMSOL simulated thermal maps of the four different microheater designs: a) meander, b) fan, c) spiral and d) S-shape

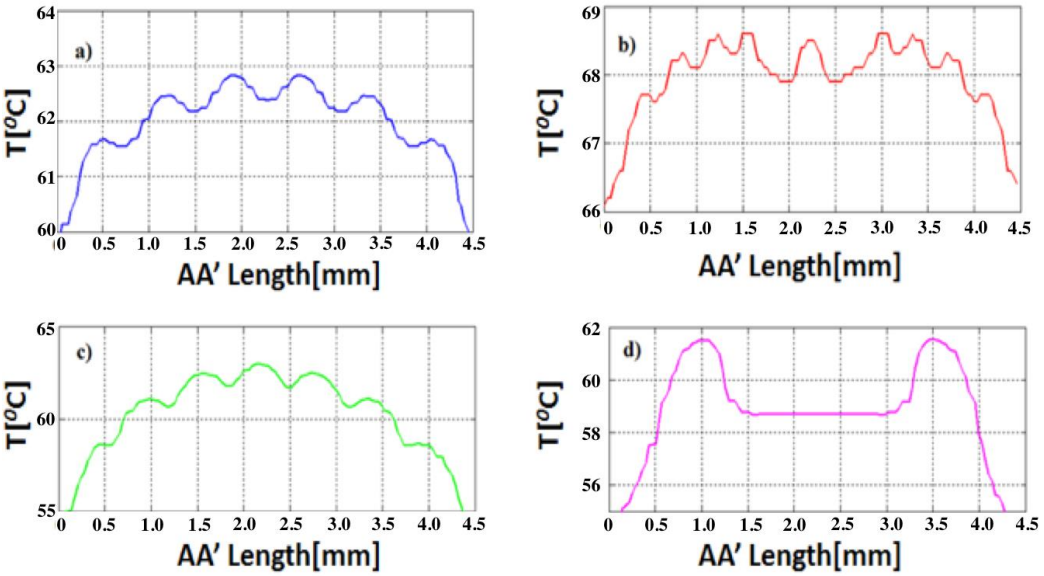

Fig 5. Temperature transverse profile of the microheater designs along AA' at 300mW: a) meander, b) fan, c) spiral and d) S shape.

In particular, in Fig.5 the temperature profiles along the line AA' obtained for an applied power of 300mW are shown. It can be observed, due to their different geometries, each structure has different temperature profile distribution. As reported in next paragraphs, these differences have a preeminent influence on the electric field analysis and thus pyroelectric emission from the –Z surface of the crystal.

The thermal maps measurements allows measuring the temperature reached on the –Z surface of $LiNbO_3$ for different applied electrical powers. These values were compared with the experimental data and illustrated in Fig. 6.

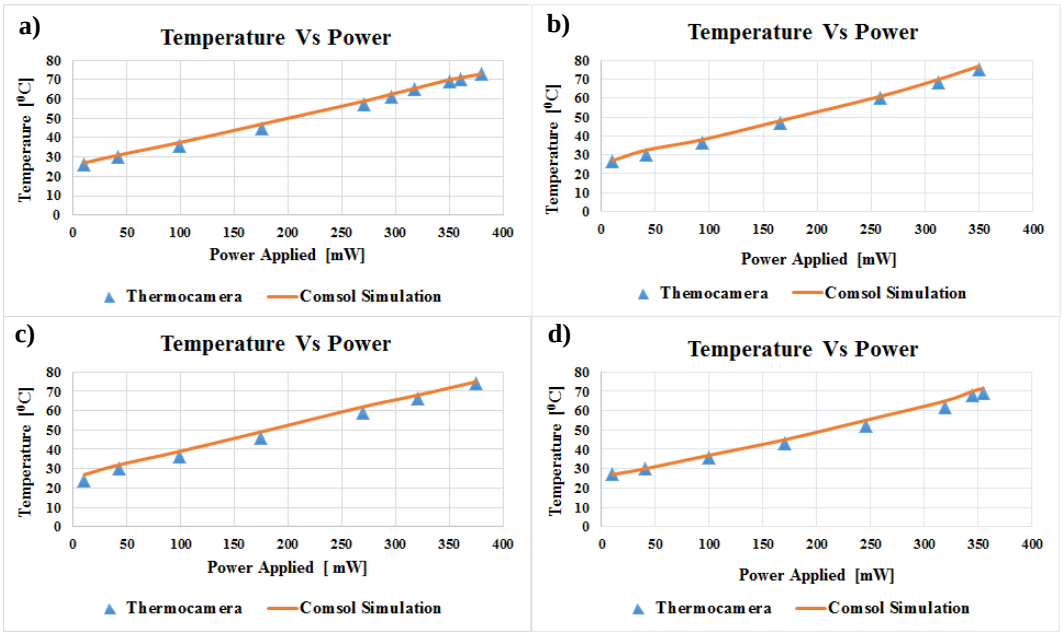

Fig 6. Temperature vs. power plot for different designs of microheaters a) meander, b) fan, c) spiral and d) S-shape estimated using simulator and observed by thermo camera.

The numerical model assumed for the microheater shows a good agreement with the experimental analysis. The maximum temperature experimentally attained on the crystal was about 75℃ for each microheater, above this temperature the crystal develops cracks initially and finally breaks. In addition to the steady state analysis, transient studies were also carried out (both experimentally and numerically) by applying an appropriate voltage square pulse waveform for 300mW electrical power with a heater-on-time of 4sec using a pulse generator. The acquired thermal maps and relative transient profile at point A' reached on –Z surface of $LiNbO_3$ using the thermal camera are shown in Fig 7 and Fig 8 respectively .

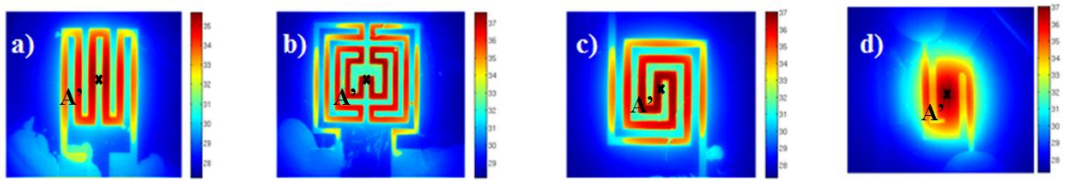

Fig 7. Thermo-camera measurement of the four different microheater designs: a) meander, b) fan, c) spiral and d) S-shape

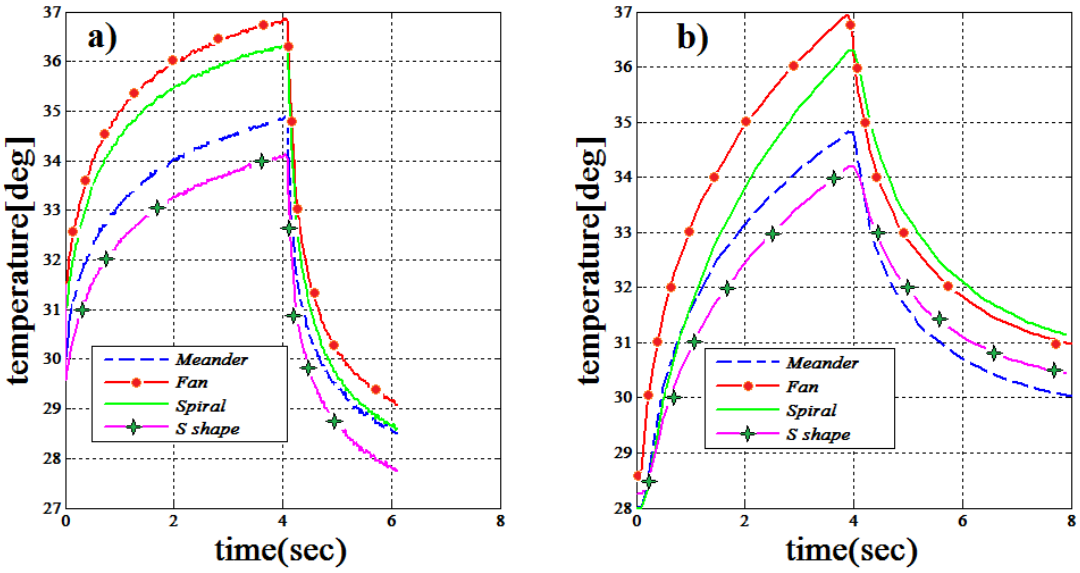

Fig 8. Experimental and simulated transient analysis of microheater designs with eater-on-time of 4sec: a) thermo camera measurement, b) COMSOL measurement.

The maximum temperature reached in transient condition for each microheater shows similar result for both simulated and experimental analyses. On the other hand, the rates of heating and cooling are different between the measured and simulated data. The different behaviour could be explained with the experimental conditions used to perform the experimental measurement. In particular, the contact and thermal resistance between the pads and connecting wire, humidity and room temperature. In Table III the extracted time constant for the heating and cooling phase are reported

	Heating	Cooling
Meander	2 sec	0,41 sec
Fan	3,2 sec	0,40 sec
Spiral	2 sec	0,39 sec
S-Shape	2 sec	0,1 sec

Table III. Time constant for the heating and cooling phase

Heating and cooling basically depends on the heat exchange between the microheater and the environment source (air). The rate of cooling is faster since the temperature differential between the air and the heated microheater is very high resulting in the higher heat exchange, while rate of heating is slower resulting in the low heat exchange during process.

b. *Electric field analysis*

The electric field strength between the –Z surface of the $LiNbO_3$ crystal and the metallic probe was simulated setting a gap of 100µm from –Z surface crystal immersed inside an air block (see Fig. 2). Heat transfer in fluid interface was considered for the block of air with an absolute pressure of 1atm. The electric field strength and the respective temperature distribution obtained by the microheaters at 300mW electrical power along the XY cut-plane are shown in Fig. 8.

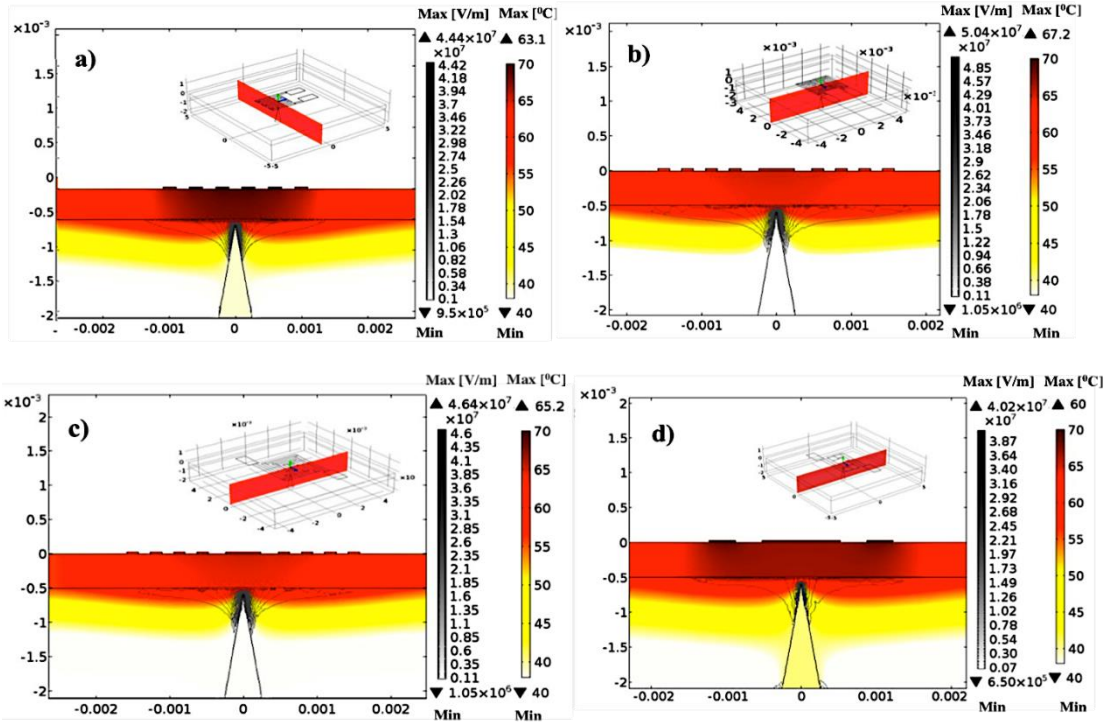

Fig 8: Electric field analysis along the XY plane (inset images) of each microheater designs: a) meander, b) fan, c) spiral and d) S shape.

It was observed that the fan shape microheater yield to have a higher electrical field strength for applied electrical power of 300mW compare to the other designs, this behaviour is attributed to the temperature transverse profile distribution due to different shape and the spacing between the heater tracks (see Fig. 5) [29].

Electric field strength was further analysed at different tip to –Z surface of $LiNbO_3$ gap spacing. A parametric sweep simulation was performed at different tip distances from the –Z surface of $LiNbO_3$ in range between 0.1mm to 1mm. The maximum value in plotted in Fig. 9 for all four microheaters. The electric field decrease with the increase in the gap spacing between the tip and –Z surface of the crystal.

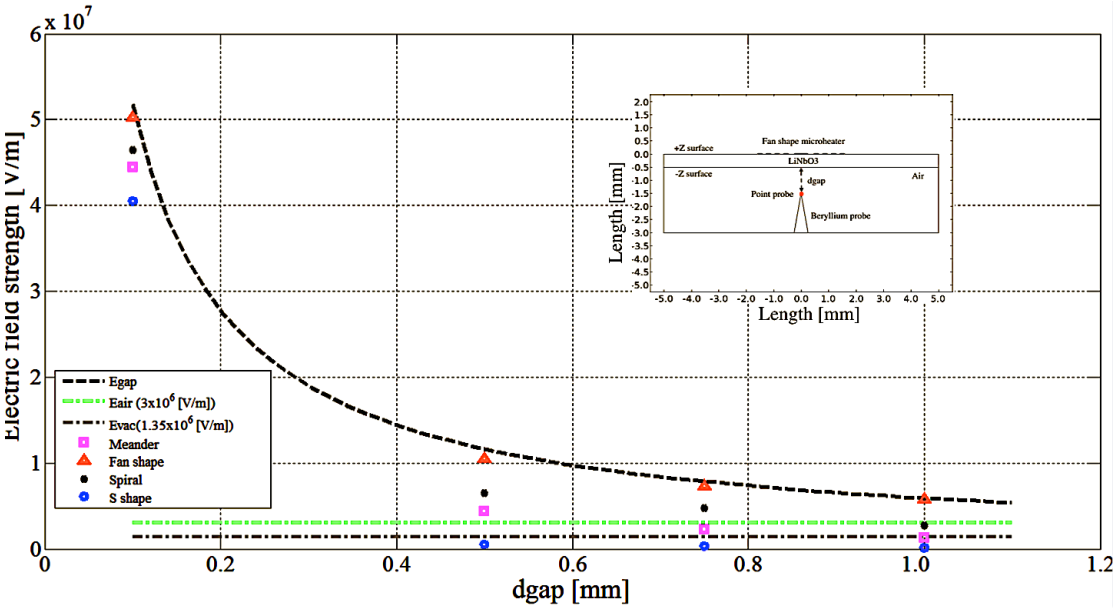

Fig 9. Electric field vs. probe tip to surface gap spacing for the microheater designs.

In the same figure, the electrical field threshold needed to induce the air (E_{air}=3x10^6 V/m) or vacuum (E_{vac}=1.35x10^6 V/m) breakdown is reported. Moreover, as upper limit, the electrical field (E_{gap}) as function of the gap spacing in vacuum condition is reported. This field can be estimated using the equation 3 [30]; i.e:

$$E_{gap} = \frac{\gamma \cdot (T_{amb} + \Delta T)}{\varepsilon_0} \cdot \left[\frac{1}{1 + \left(\frac{d_{gap}}{d_{cr}}\right) * \varepsilon_{cr}} \right] \quad \text{.....(3)}$$

Where, ε_0 is the permittivity of free space, *dgap* is the tip to sample distance, T_{amb} is the room temperature (27°C) and ΔT is the temperature variation induced by the microheaters driven with an electrical power of 300mW. These simulation data, according to the microheater shape, allow evaluating the tip-to-surface gap needed to induce an air breakdown. For example, a fan microheater driven with an electrical power of 300mW can induce an electrical field on the pyroelectrical crystal enough strength to cause the air breakdown for gap spacing lesser than 1mm. Whereas for a meander microheater the gap has to be lesser than 0.5mm.

IV. Pyroelectric effect analysis of $LiNbO_3$ crystal

In order to evaluate the pyroelectric effect, the setup schematically illustrated in Fig 10 was adopted. In particular, a 10mm × 10mm × 500µm pyroelectric $LiNbO_3$ sample with the afore-described microheaters on the +Z face, was mounted with the –Z face exposed to a suspended metallic tip used to monitor electrical activity on the crystal surface. The $LiNbO_3$ +Z surface is heated by the fabricated microheater. Microheater is driven by a periodic pulse waveform, while a metallic tip is placed near the –Z face to monitor the pyroelectric effect using an oscilloscope.

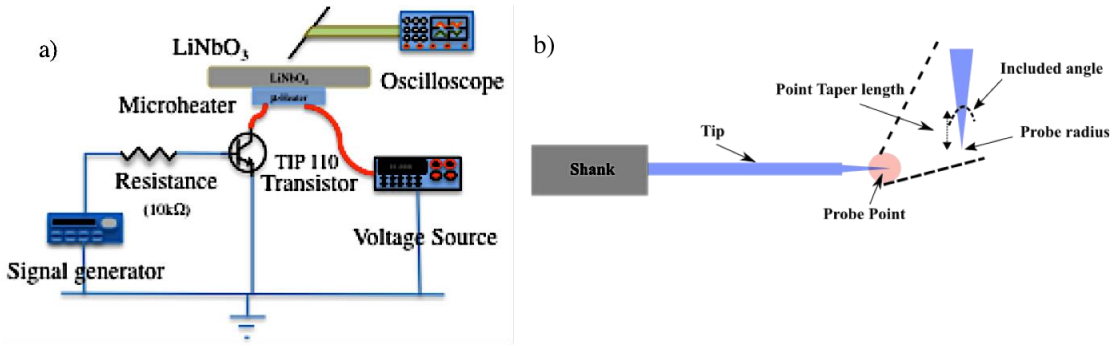

Fig 10. a) Schematic of experimental setup; b) Schematic of the tip probe

When the temperature of the sample is stationary, the polarization of the pyroelectric material is compensated by free charges (electrons or ions) from the ambient condition [19, 30,31]. If a voltage is applied to the microheater, during the transient an electrical power is dissipated in the form of heat and thus the temperature of the crystal increases. Consequently, the spontaneous polarization decreases and net surpluses of compensating positive charge on the –Z face are obtained. Thus, an electrical field is induced between the –Z face and the point like metallic tip. This field charges the interelectrode capacitance, which includes the parasitic capacitances and the oscilloscope capacitance. If the electrical field is enough strong to induce an air breakdown, the interelectrode capacitance can discharge themselves through the low impedance formed by the discharge between the metallic tip and the –Z face. The oscilloscope records the voltage drop at breakdown and a negative current impulse is observed. As the microheater is switched off, the cooling transient induces an increase in polarization and net deficits of compensating positive charge on the -Z face. Thus, a positive current impulse can be observed at the oscilloscope. Obviously, the impulse occurrence is strictly dependent on gap-spacing distance between the crystal surface and the metallic tip. In particular, the induced electrical field as function of the gap spacing that can be estimated by equation (3)[30,32].
In our experiment, the metallic tip was positioned on the –Z face in the centre of the area heated by the microheater where the temperature variation is higher and thus the pyroelectric effect is greater (see Fig. 10).

The microheaters were driven with a periodic square waveform with a frequency of 10mHz, and a voltage adjusted to dissipate an electrical power of 300mW for each microheater. The periodicity of the applied voltage was useful to see the pyroelectric current using the oscilloscope, and to detect the repeatability of the induced pyroelectric effect. The frequency of the waveforms was chosen in order to allow both the thermalization of the pyroelectric crystal during the heating phase and the natural cooling of the pyroelectric material after the switching off of the microheater. As results from Fig. 5, for the applied electrical power the temperature of the –Z face was about 60°C. The distance between the tip and the –Z face was set to 100µm. The picked up waveforms for each microheater are reported in Fig11.

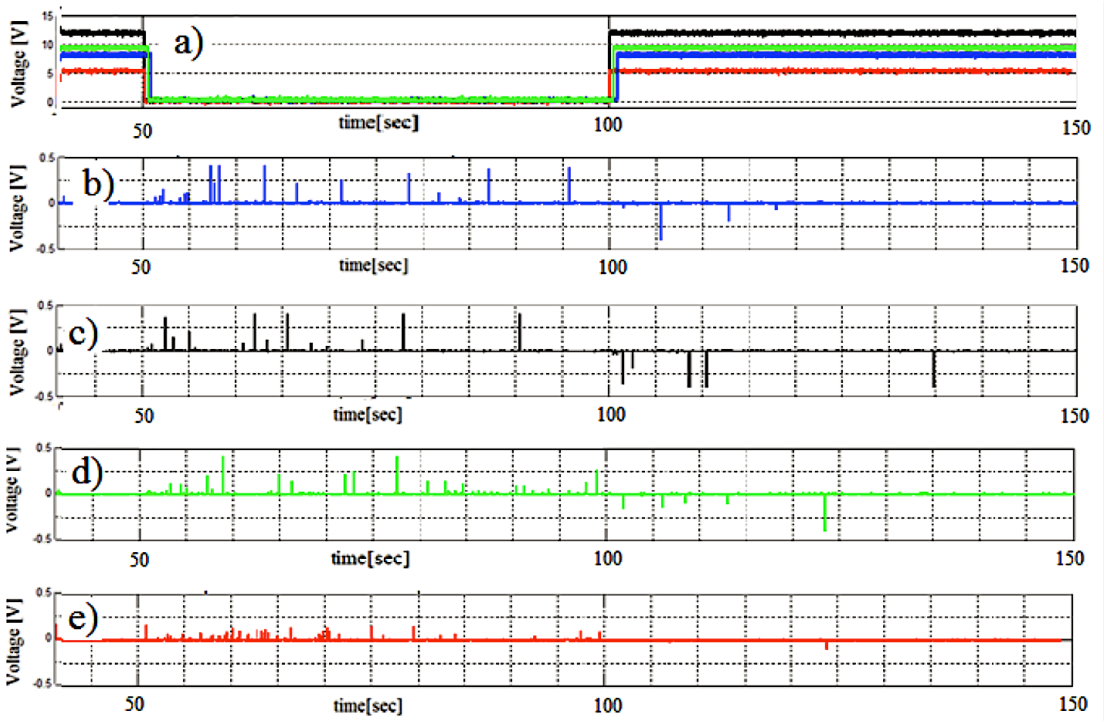

Fig 11. Current impulses obtained for different designs of microheater: a) applied voltage signal to dissipate a power of 300mW at 10mHz b) meander c) fan d) spiral and d) S-shape.

Higher electric field strength results in the larger amplitude (> 250mV) of current impulses for the fan shape microheater, while lower amplitude (<150mV) of current impulses was obtained in the S shape microheater see Fig. 9.

When the microheater is turned on (off), an exponential heating (cooling) of the structure is activated (see Fig. 7). So, a quick change in the rate of change of the temperature is initially induced, causing acceleration in spontaneous polarization variation. As consequence, air breakdown and consequently the occurrence of the current impulses can be happening very often. On the other hand, when the structure is approaching the thermalization, the rate of change of the temperature is slower, and as consequence, current impulses are sparser. Because the cooling phase is faster than the heating one (see Table III), in the same period of time, the pyroelectric effect induced in the cooling phase is greater than that one induced in the heating phase. Thus, a larger net surpluses of compensating positive charge on the –Z face are obtained during the cooling phase; as consequence, more impulses are obtained in the cooling period.

Fig. 12 shows the temporal distance trend between two consecutive electrical impulses during the whole thermal transient. This temporal distance is very short during the initial phase of the thermal transient, while grows when complete thermalization of the sample is reaching. The reported data are relative to a fan-shaped microheater with the probe at 100µm gap spacing, but similar results were observed for the other designs. The fitting curve clearly shows the exponential dependence of the occurrence of the electrical impulses (i.e. the pyroelectric effect) on the thermalization of the crystal induced by the microheater. Moreover, the steeper slope in the cooling condition of microheater confirms that the rate of cooling is faster than the heating condition.

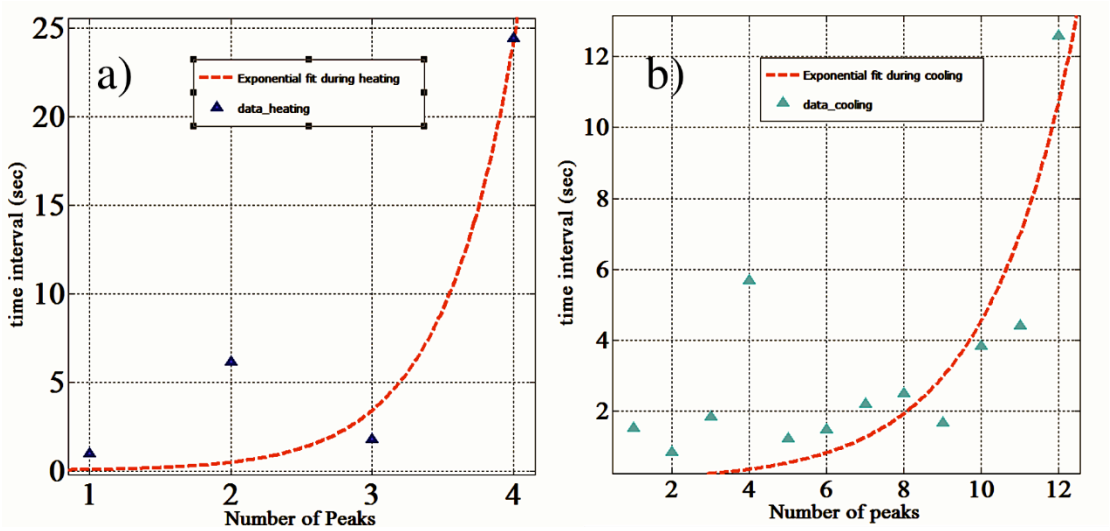

Fig 12. Temporal distance between two consecutive electrical impulses during the: a) heating condition, b) cooling condition.

The PE as function of the gap between the surface and the metallic tip was analysed. In particular, a micromanipulator was adopted for varying the tip-surface gap spacing from 100µm to 1mm. The measurements reported in Fig. 13 were performed on fan-shape-based structure by applying a square voltage signal useful for dissipating an electrical power of 300mW at 10mHz frequency.

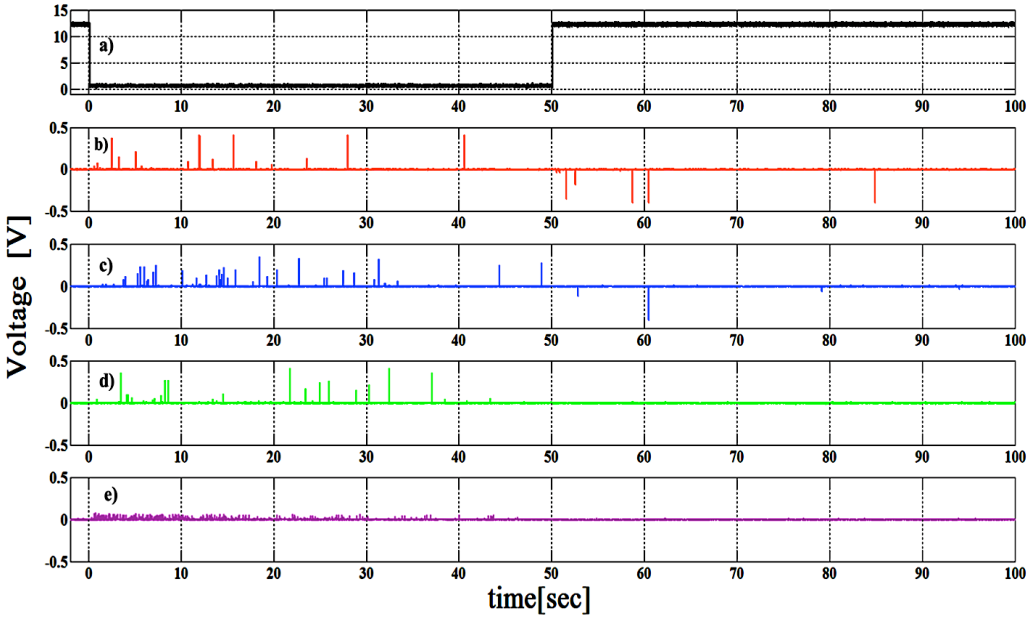

Fig 13. Current impulses at different gap spacing: a) the applied signal to fan shape microheater, the impulses obtained at b) 0.1(mm), c) 0.5(mm), d) 0.75(mm), e) 1(mm).

During natural cooling (occurring after turning off the heater), current impulses of amplitude approximately greater than 250mV were observed for distances from the –Z surface of crystal ranging from 100µm to 750µm; whereas, lower amplitudes (< 100mV) were detected for d_{gap} > 750µm. Finally, as the tip is moved farther from the –Z surface of crystal, the induced electric field decreases at very low values and only few impulses with low amplitudes are present. The experimental results are slightly different from the simulation ones reported in Fig.9, because the simulations didn't take into account the presence of free charges around the crystal surface that compensate the polarization charges induced by the pyroelectric effect.
A similar behaviour was observed during the heating phase, even if the slower trend of this phase induces a weak pyroelectric effect resulting in a few number of current impulses with a small amplitude for a gap spacing < 500µm and no impulses for d_{gap} >500µm.
One of the main advantages of heating by means of an integrated microheater is the high controllability of the heating process and so of the pyroelectric effect. For example, during either the heating or cooling phase, the occurrence of the impulses (i.e. the time shift between the applied voltage switching and the observed impulses) was obtained with a great regularity. In Fig. 14 a statistic of the occurrence of the first impulse during heating and cooling phases for a fan shaped microheater is reported.

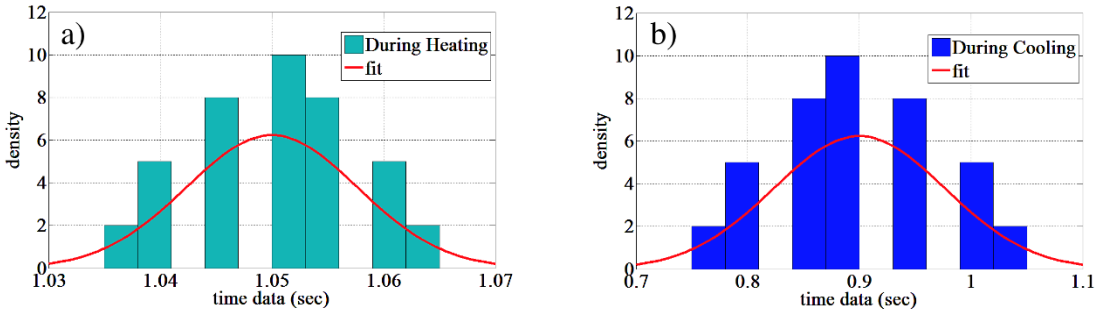

Fig 14. Occurrence of the first impulses with respect to delay time: a) during heating, b) during cooling.

The mean value and the variance of the Gaussian distribution are 1.05sec (0.9sec) 5.9ms (59µs) during the heating (cooling) condition, respectively. The first impulse during the cooling phase occurs faster than the impulse during heating phase thanks to the quicker rate of change in the temperature in cooling condition. In Fig. 15 the occurrence of the first impulse as a function of the driving signal frequency (from 10mHz to 100mHz) and electrical power applied to the microheater (200mW, 250mW and 300mW) is illustrated. The shown data are relative to a fan-shaped microheater, but analogous results were also obtained for the others designs.

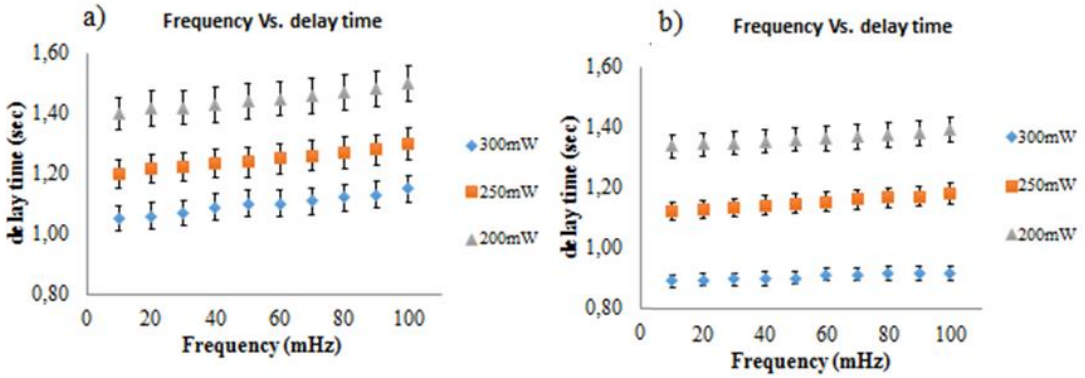

Fig 15. Delay time vs. frequency for different dissipated electrical power during: a) heating condition b) cooling condition.

The delay time for the initial occurrence of the peaks during natural cooling conditions remains more of less the same while in the heating phase a small drift is observed at different frequencies. This drift is related to the heat accumulation induced by the highest frequencies. The investigation demonstrates that the occurrence of the initial PE from the crystal can be governed by controlling electrical power (thus controlling the rate of heating and cooling) applied to microheater.

Humidity measurements

The pyroelectric effect activated by the fan microheater was investigated analyzing the pyroelectrical current impulses detected using a micrometric metallic probe connected to an oscilloscope under humid conditions. In particular, the temperature variation due to the microheater induces a spontaneous polarization change, which produces a redistribution of the bound charges on the crystal surface. A resistive Aluminum Sensor was integrated along the microheater in order to control the temperature variation effect from the microheater. The electrical field generated between the crystal surface and the metallic probe causes an air breakdown that appears as an impulse on the oscilloscope. In this work, the pyroelectric current impulses was analyzed for the fan microheater design and operating conditions (Humidity) in order to demonstrate the effectiveness of the microheater as thermal tool for activating the pyroelectric effect. Fabrication of the fan shape microheater and the respective resistive thermal sensor was performed using photolithography process and metal deposition technique [34].

The step process involve in the photolithography and metal deposition process with the obtained fabricated output is shown in fig 16:

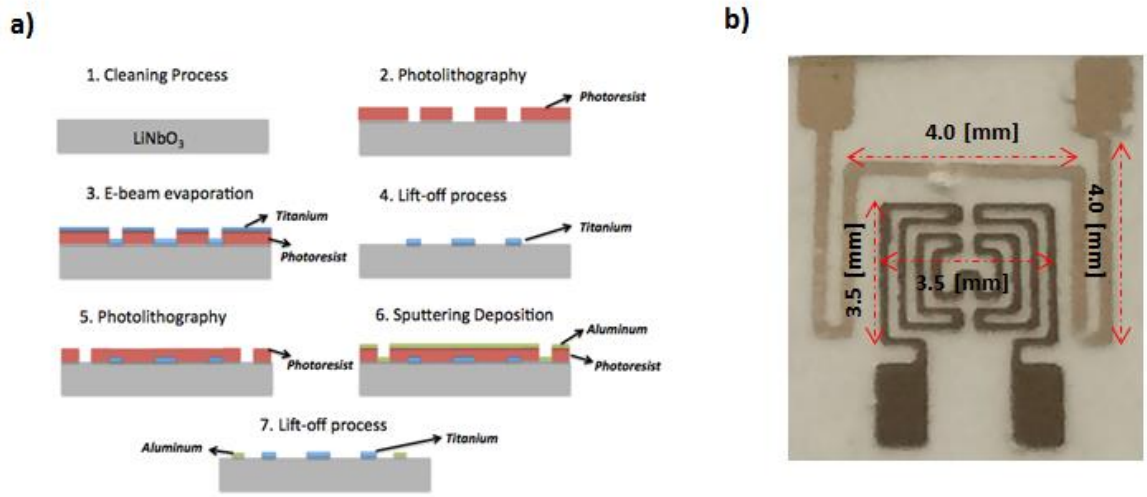

Fig 16: a) Photolithography and metal deposition process flow, b) fabricated microheater with sensor on $LiNbO_3$.

Titanium (Ti) of 300nm-thick was the choice for heater material and Aluminum (Al) of 200nm was used for the resistive sensor. Titanium & aluminum was deposited using electron beam and sputtering technologies. Finally the pads of the microheater and thermal sensor were wire bonded using silver paste. The measured microheater resistance was 820Ω and the Aluminum sensor was 36.7Ω respectively.

Thermal analysis of the Microheater

Thermal analyses of the titanium microheater designs were performed both theoretically and experimentally, using COMSOL ™ Multiphysics package and thermal sensor. The thermal sensor was bonded on the -Z surface in the center of the area heated by microheater where the temperature variation is higher using a silver paste. The integrated aluminum resistive sensor was neglected, while performing the theoretical simulation using COMSOL multiphysics. The obtained temperature on both the thermos couple and the respective change of the resistance of the integrated resistive sensor with respect to the electric power applied on the microheater is shown in fig 17.

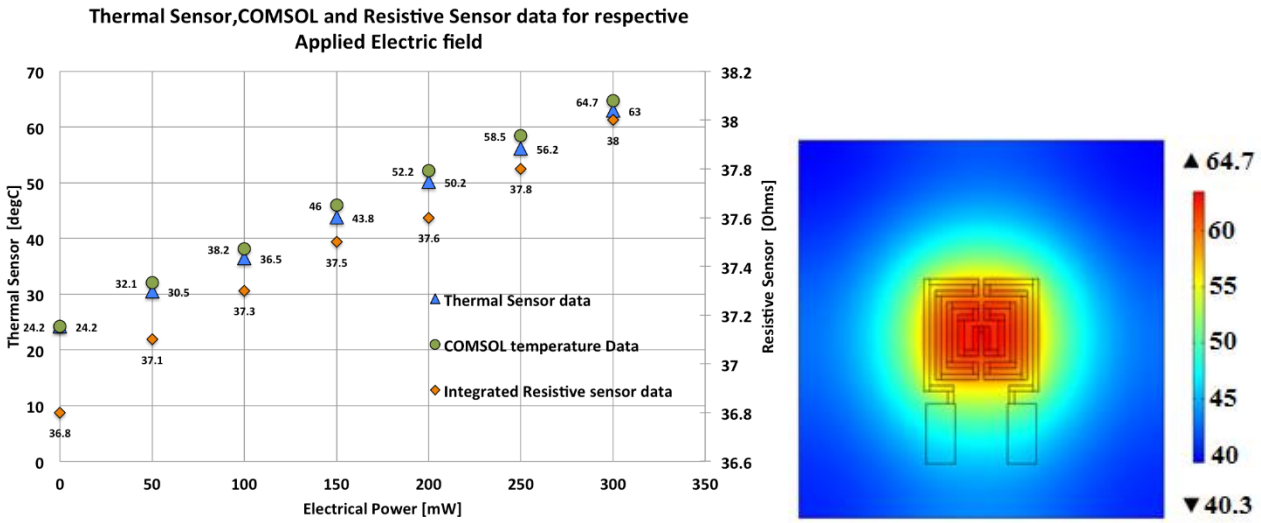

Fig 17: a) Temperature and resistance measurement from thermo couple sensor, COMSOL & resistive sensor at different applied electric power to microheater, b) COMSOL thermal Map of Fan Shape Microheater at 300mW applied electrical power.

A transient investigation was also further analyzed by applying a step voltage in order to dissipate an electrical power of 300mW for 10 sec with 50 % duty cycle using a voltage generator. In figure 18, we observe the obtained thermal sensor plot with the respective aluminum resistive sensor data in the transient regime for the heater on and heater off time for 5 sec each.

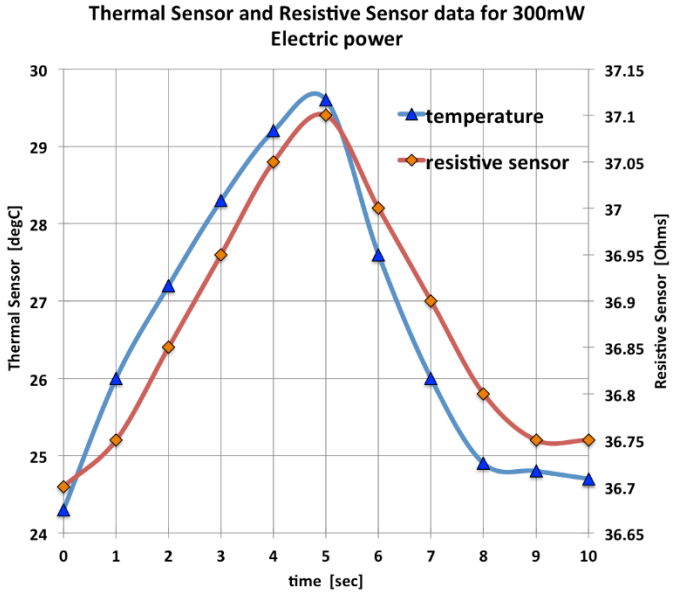

Fig 18: Transient measurement of the thermal and resistive sensor on application of 300mW electric power.

The pyroelectric effect from –Z surface of $LiNbO_3$ activated by the fan shape microheater was further investigated analyzing the pyroelectrical current impulses detected using a beryllium micrometric

probe connected to an oscilloscope. The micrometric metallic probe was positioned at 100µm gap from the –Z surface of crystal using a micromanipulator. The setup was placed inside a closed Teflon case for investigating pyroelectric effect under humid condition. The schematic of the closed case setup is shown in fig 19. The initial humidity of the closed system was measured around 54% using a RH318 (testo 525) Humidity sensor.

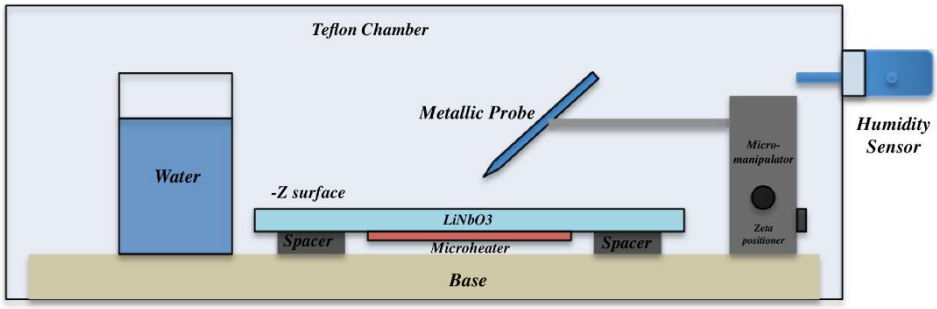

Fig 19: Schematic of the humidity measurement setup.

A periodic square waveform with a frequency of 100mHz, and a voltage adjusted to dissipate an electrical power of 300mW was applied to the microheater. The micrometric metallic probe was positioned at 100µm from the –Z surface of $LiNbO_3$ crystal for obtaining the current impulses. The variation in temperature due to the microheater induces spontaneous polarization of the crystal thus producing a redistribution of bound charges on –Z surface of crystal, hence resulting in an induced electric field due to the inter-electrode capacitance between the –Z surface and metallic probe. If the electric field is strong enough to induce an air breakdown, the inter-electrode capacitance can discharge themselves through the low impedance formed by the discharge between the –Z face and metallic probe. When the temperature of the crystal increase, the decrease in the spontaneous polarization occurs and results in the net deficits of compensating negative charges on the –Z surface of crystal. Thus, negative current impulses can be observed at the oscilloscope and vice-versa. The surface bounds charges play an important role in generating the current peaks on the oscilloscope. These bound charges response to the motion of charge particles in the air dielectric film between crystal surface and metallic probe. Controlling the humidity of the surrounding can regulate the motion of charge particles in the air. In order to reduce the humidity of the closed system 150gms of bay salt was placed in a container and inserted in the closed Teflon case system. The humidity was reduced from 54% to 42%.

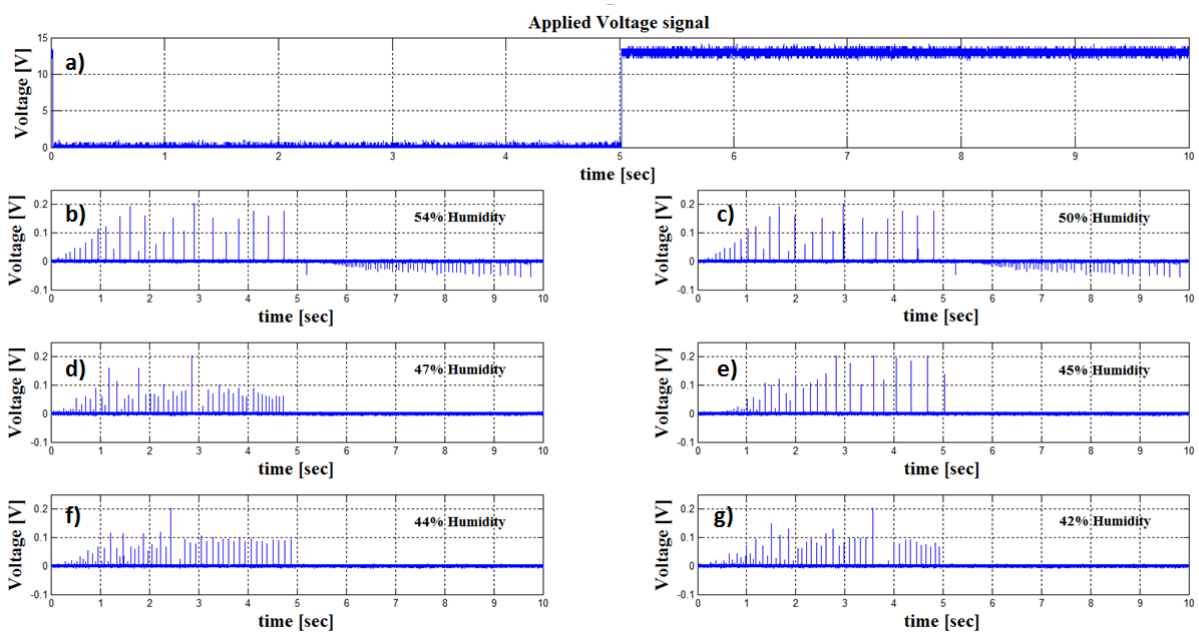

Fig 20: Current peaks obtained on oscilloscope using metallic probe: a) Voltage signal applied to microheater to dissipate electrical power of 300mW, b) 54% Humidity, c) 50% Humidity, d) 47% Humidity, e) 45% Humidity, f) 44% Humidity and g) 42% Humidity.

It was observed, as the humidity of the system decrease thus the density of air increase resulting in the reduction of the air resistance against the motion of particles making the dielectric of air less conductive inside the closed case. Thus the electric field required for the dielectric breakdown of air to produce the current peaks increases. This results in the obtaining lower current peaks on the oscilloscope during heating, while during the cooling a faster rate of change in temperature dominating the humidity effect resulting in more number but with lower amplitude of voltage peaks compare to heating.

References:

1) Coates, P. B. (1981). Multi-wavelength pyrometry. *Metrologia* , *17*, 3.
2) Fujitsuka, N., Sakata, J., Miyachi, Y., Mizuno, K., Ohtsuka, K., Taga, Y., Tabata, O. (1998). Monolithic pyroelectric infrared image sensor using PVDF thin film. *Sensor and Actuators A:Physical* , *66* (1-3), 237-243.
3) Lang, S. B. (2005, august). Pyroelectricity: From ancient curiosity to modern imaging tool. *Physics Today* , 31-36.
4) Lehman, J., Eppeldauer, G., Aust, J. A., Racz, M. (1999). Domain-engineered pyroelectric radiometer. *Applied Optics* , *38* (34), 7047-7055.
5) Kim, D. W., Moon, C. W., and Yoo, I. K. (2003). Pyroelectric Emission Lithography. *Journal of the Korean Physical Society* , *42*, s1196-s1198.

6) Moon, C. W., Kim, D.-W., Rosenman, G., Ko, T. K., and Yoo, I. K. (2003). Patterned Pyroelectric Electron Emitters and their Feasibility Study for Lithography Applications. *Japanese Journal of Applied Physics , 42*, 3523.
7) Coppola, S., Vespini, V., Grilli, S., and Ferraro, P. (2011). Self-assembling of multi-jets by pyro-electrohydrodynamic effect for high throughput liquid nanodrops transfer. *Lab on a Chip , 11*, 3294-3298.
8) Rosenman, G., Shur, D., and Skliar, A. (1996). Ferroelectric electron emission flat panel display. *Journal of applied physics , 79*, 7401.
9) N. Balcon, D. Payan, M. Belhaj, T. Tondu and V. Inguimbert, "Secondary Electron Emission on Space Materials: Evaluation of the Total Secondary Electron Yield From Surface Potential Measurements," in *IEEE Transactions on Plasma Science*, vol. 40, no. 2, pp. 282-290, Feb. 2012.
doi: 10.1109/TPS.2011.2172636
10) Neidholdt, L. E., and Beauchamp, L. J. (2007). Compact ambient pressure pyroelectric ion source for mass spectrometry. *Analytical chemistry , 79*, 3945-3948.
11) Neidholdt, E. L., and Beauchamp, J. L. (2009). Ionization mechanism of the ambient pressure pyroelectric ion source (APPIS) and its applications to chemical nerve agent detection. *J Am Soc Mass Spectrom , 20*, 2093-2099.
12) Gennari, O., Grilli, S., Coppola, S., Pagliarulo, V., Vespini, V., Coppola, G., Bhowmick, S., Gioffré, M.A., Gentile, G., Ambrogi, V., Cerruti, C., Carfagna, C., Ferraro, P. (2013). Spontaneous assembly of carbon-based chains in polymer matrix through surface charge templates. *Langumir , 29*, 15503-15510.
13) Ferraro P., Coppola S., Grilli S., Paturzo M. and Vespini V. (2010). Dispensing nano–pico droplets and liquid patterning by pyroelectrodynamic shooting. *Nature Nanotechnology*, 5, 429–435, doi: 10.1038/nnano.2010.82.
14) Vespini, V., Coppola, S., Grilli, S., Paturzo, M., and Ferraro, P. (2013). Milking liquid nano-droplets by an IR laser: a new modality for the visualization of electric field. *Meas. Sci. Technol.*, 24 045203, doi: 10.1088/0957-0233/24/4/045203.
15) Mecozzi, L., Gennari, O., Rega, R., Grilli,S., Bhowmick, S., Gioffrè,M.A., Coppola, G., Ferraro,P. (2016). *Spiral formation at the microscale by µ-pyro-electrospinning.* Soft matter, DOI: 10.1039/c6sm00156d
16) Coppola, G., Sirleto, L., Rendina, I., and Iodice, M. (2011). Advance in thermo-optical switches: principles, materials, design, and device structure. *Opt. Eng*., 50(7), 071112.
17) Chul ha, S., Kim, Y. S., Yang, Y., Kim, Y. J., Cho, S.M., Yang, H., Kim, Y.T. (2005). Integrated and Micro-Heater embedded gas sensor array based on the polymer composites dispensed in micromachined wells. *Sensors and Actuators B:Chemical , 105* (2), 549-555.
18) Neda, T., Nakamura, K., and Takumi, T. (1996). A polysilicon flow sensor for gas flow meters. *Sensor and actuators A: Physical , 54* (1-3), 626-631.
19) Velmathi, G., Ramshanker, N., and Mohan, S. (2010). 2D simulations and electro-thermal analysis of Micro-Heater design using COMSOL for gas sensor applications. *COMSOL conference*, India.
20) Rosenman, G., Shur, D., Krasik, Y., and Dunaevsky, A. (2000). Electron emission from ferroelectrics. *Journal of Applied physics , 88*, 6109.
21) Grilli, S., Coppola, S., Vespini, V., Merola, F., Finizio, A., Ferraro, P. *(2011)*. 3D lithography by freezing liquid instabilities at nanosclae. *PNAS*, 108-15106.

22) Mahony, C. O., Hill, M., Hughes, P. J., and Lane, W. A. (2002). Titanium as a micromechanical material. *Journal of micromechanics and microengineering , 12*, 438-443.
23) Comsol A. *COMSOL multiphysics user's guide*.
24) Peirs, J., Reynaerts, D., and Brussel, H.V. (1998). Scale effects and thermal considerations for micro-actuators. *International conference on Robotics and Automation*, Leuven Belgium.
25) Asheghi, M., Leung, Y.K., Wong, S.S., and Goodson, K.E. (1997). Phonon-boundary scattering in thin silicon layers. *Applied Physics letters*, vol. 71, p. 1798.
26) Lacy, F. (2011). Developing a theoretical relationship between electrical resistivity, temperature, and film thickness for conductors. *Nanoscale Research Letters*, p. 6:636.
27) Thuau, D., Koymen, I., Cheung, R., (2011). A microstructure for thermal conductivity measurement of conductive thin films. *Microelectronics engineering*, 88, 2408-2412.
28) M. Riccio, A. Pantellini, A. Irace, G. Breglio, A. Nanni, C. Lanzieri, Electro-thermal characterization of AlGaN/GaN HEMT on Silicon Microstrip Technology, Microelectronics Reliability, Volume 51, Issues 9–11, September–November 2011, Pages 1725-1729, ISSN 0026-2714, http://dx.doi.org/10.1016/j.microrel.2011.07.003.
29) G. Romano, M. Riccio, G. De Falco, L. Maresca, A. Irace and G. Breglio, "An ultrafast IR thermography system for transient temperature detection on electronic devices," 2014 Semiconductor Thermal Measurement and Management Symposium (SEMI-THERM), San Jose, CA, 2014, pp. 80-84. doi: 10.1109/SEMI-THERM.2014.6892219
30) Darhuber, J. P. Valentino, S. M. Troian and S. wager, (2003). Thermocapillary actuation of droplets on chemically patterned surfaces by programmable Micro-Heater arrays. *Journal of Microelectromechanical systems*, vol. 12, p. 6.
31) Shur, D., and Rosenman, G., (1996). Figures of merit for ferroelectric electron emission cathodes, *Journal of Applied Physics*, **80**(6), 3445.
32) Kim, D.-W., Bourim, E.M., Jeong, S.-H., and Yoo, I.K., (2004). Pyroelectric electron emission and domain inversion of LiNbO3 single cystal, *Physica B*, vol. 352, pp. 200-205.
33) Bourim, E.M., Moon, C.-W., Lee, S.-W., Sidorkin, V., and Yoo, I.K., (2006). Pyroeletric electron emission from -Z surface polar surface of Lithium nionbate monodomain single crystal, *J Electroceram*, vol. 17, pp. 479-485.
34) Bhowmick, S., Iodice, M., Gioffrè, M., Breglio, G., Riccio, M., Irace, A., Romano, G., Coppola, G. (2015). "Pyro-Electro-Thermal analysis of $LiNbO_3$ using microheaters" *Fotonica AEIT Italian Conference on Photonics Technologies, 2015*, Turin, 2015, pp. 1-5. doi: 10.1049/cp.2015.0129.

List of publications

i. **S. Bhowmick**, M. Iodice, M. A. Gioffrè, G. Breglio, A. Irace, M. Riccio, G. Romano, S. Grilli, P. Ferraro, L. Mecozzi, S. Coppola, O. Gennari, R. Rega, G. Coppola
"Investigation of Pyroelectric fields generated by Lithium Niobate crystals through integrated microheaters**"**
Journal of applied Physics,

ii. L. Mecozzi, O. Gennari, R. Rega, S. Grilli, **S. Bhowmick**, M. A. Gioffrè, G. Coppola, P. Ferraro
"SPIRALS FORMATION AT MICROSCALE BY µ- PYROELECTROSPINNING"
Soft Matter, May 2016, DOI: 10.1039/C6SM00156D

iii. O. Gennari, S. Grilli, S. Coppola, V. Pagliarulo, V. Vespini, G. Coppola, **S. Bhowmick**, M. A. Gioffrè, V. Ambrogi, P. Cerruti, C. Carfagna, P. Ferraro
"SPONTANEOUS ASSEMBLY OF CARBON-BASED CHAINS IN POLYMER MARTIXES THROUGH SURFACE CHARGE TEMPLATES"
Langmuir December 2013, 29, pp. 15503-15510, DOI: *10.1021/la403603d.*

Conference Proceedings

i. **S Bhowmick**, M Iodice, M Gioffrè, G Breglio, M Riccio, A Irace, G Romano, G Coppola:
"*Pyroelectric effect Investigation on $LiNbO_3$ crystal under humidity conditions using Microheater*"**.**
11th IEEE Nanotechnology Materials and Devices Conference (2016), Toulouse, France.
DOI: 10.1109/NMDC.2016.7777087

ii. L. Mecozzi, O. Gennari, R. Rega, S. Grilli, **S. Bhowmick**, M. A. Gioffrè, G. Coppola, P. Ferraro
"*SPIRAL FORMATION AT MICROSCALE BY M-PYRO-ELECTROSPINNING"*
AIP Conference Proceedings 1736, 020079 (2016); Naples, Italy.

iii. **S. Bhowmick**, M. Iodice, M.A. Gioffrè, G. Breglio, M. Riccio, A. Irace, G. Romano, G. Coppola
"*PYRO-ELECTRO-THERMAL ANALYSIS OF LINBO3 USING MICROHEATERS"*
Fotonica AEIT Italian Conference on Photonics Technologies (2015), Turin, Italy.

iv. **S. Bhowmick**, O. Gennari, S. Grilli, V. Vespini, G. Gentile, V. Ambrogi, P. Cerruti, M. A. Gioffrè, C. Carfagna, P. Ferraro, S. Coppola, V. Pagliarulo, G. Coppola

"*CARBON BASED WIRES ASSEMBLING USING PYROELECTRIC EFFECT CONTROLLED BY MEANSOF TITANIUM M-HEATERS"*

1st EOS Topical metting on Optical Microsystems (OμS' 13), Capri, Italy